ACS APPLIED NANO MATERIALS

www.acsanm.org

Article

Nanostructured Layered Lithium Iridates as Electrocatalysts for Improved Oxygen Evolution Reaction

Francisco Gonell,* Gwenaëlle Rousse, Mateusz Odziomek, Walid Baaziz, Ovidiu Ersen, Alexis Grimaud, and Clément Sanchez*

Cite This: *ACS Appl. Nano Mater.* 2023, 6, 2577−2584

Read Online

ACCESS | Metrics & More | Article Recommendations | Supporting Information

ABSTRACT: We report for the first time the synthesis pathway of nanostructured lithium iridates in molten salts with tunable particle and crystal sizes. The structural analysis confirms that these materials are phase-pure, with a layered α-Li_2IrO_3 structure and a surface area 2 orders of magnitude higher than that of the materials obtained by traditional solid-state methodology. Improved OER activities were obtained compared to the bulk counterpart, given the improved surface area. Intriguingly, the electrocatalytic behavior of this nanoscaled α-Li_2IrO_3 significantly differs from the bulk counterpart. Such a different behavior may arise from the small size of the synthesized materials; thus, surface reactions play a key role. Additionally, the nanoscaled α-Li_2IrO_3 shows good chemical and structural stability; thus, negligible deactivation was observed in KOH and H_2SO_4 electrolytes with low electrode catalyst loading during 24 h of chronopotentiometry. Besides this stability, these materials show enhanced iridium intrinsic activity with 336 and 181 A g_{Ir}^{-1} in H_2SO_4 and KOH electrolytes, respectively. This work shows how the design of high-temperature colloidal synthesis yields nanoscaled materials with enhanced and different electrocatalytic properties compared to bulk counterparts and pave the way to the design of electrocatalysts with enhanced mass activity.

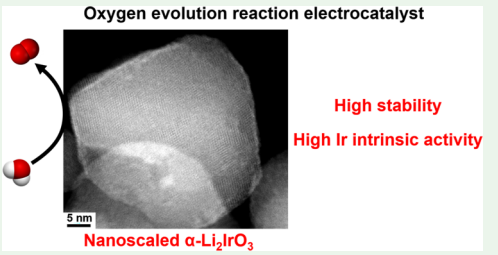

KEYWORDS: *lithium iridate, nanomaterials, molten salts, electrocatalysis, oxygen evolution reaction, layered materials*

INTRODUCTION

The increasing world energy demand requires environmentally friendly alternatives to traditional energy sources based on finite fossil fuels. Electrolysis has emerged as one of the most promising strategies in order to transform renewable energy into chemical bonds, so that energy can be stored in the form of molecules and used on demand. Hydrogen-based technologies show an incipient maturity with electrocatalysts able to reduce water at low overpotentials. Nevertheless, the implementation of hydrogen produced from the electrolysis of water is hampered by the other half-reaction, namely oxygen evolution reaction (OER), which still requires the application of a much greater overpotential to achieve sufficient current density. Additionally, the most efficient catalysts are based on expensive ruthenium and iridium oxides, which demand strategies to optimize and increase the number of active sites per gram besides improving the durability.

Among the iridium-based oxides, lithium iridates are interesting materials because of the rich composition chemistry showing 2D polymorphs such as α-Li_2IrO_3, Li_3IrO_4, or 3D structures such as β-Li_2IrO_3 or γ-Li_2IrO_3. Some of these materials have been studied as model compounds as cathodes in lithium ion batteries, developed to explain the high capacity observed in more complex cathode materials arising from cationic and anionic reversible processes.[1−3] When cycled in aqueous electrolytes containing species such as protons or potassium, cations were shown to insert in the structure after initial activation/delithiation, rendering new highly active and stable structures for OER.[4,5]

The traditional synthesis of lithium iridates is based on solid-state methodology employing metallic iridium or iridium oxide precursors and a slight excess of lithium salt which are grinded and fired at high temperatures for long periods.[1,2] The products obtained show big crystal and particle sizes and as a consequence low surface area values (below 0.1 m^2 g^{-1}).[5] The synthesis of these materials in the nanoscale has never been explored despite the promise of new and enhanced properties derived from increased surface effects, as a consequence of the increment in the number of defects and exposed surface atoms, at the expense of bulk ones. The high synthesis temperatures required in the solid-state process favor sintering and crystal growth precluding the nanoparticle isolation.

Molten salts are stable high-temperature liquids which are particularly suitable to perform the colloidal synthesis of

Received: November 14, 2022
Accepted: January 20, 2023
Published: February 7, 2023

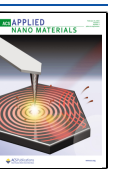

https://doi.org/10.1021/acsanm.2c04949
ACS Appl. Nano Mater. 2023, 6, 2577−2584

materials that require high temperatures to crystallize while the uncontrolled particle growth is avoided. This synthesis pathway is scalable, environmentally friendly, as the salt can be easily removed by washing and recycled, and produces highly crystalline nanomaterials with clean surfaces, with high versatility of compositions and new and enhanced properties.[6−13]

In this work, the production of lithium iridate nanomaterials with a tunable size is attempted for the first time, through the design of a high-temperature colloidal synthesis, in molten salts (Scheme 1). The derived electrochemical properties are deeply studied, shedding light into the dependence of these properties by decreasing the particle size.

Scheme 1. Schematic Representation of the Molten Salt Synthesis of Nanoscaled α-Li_2IrO_3

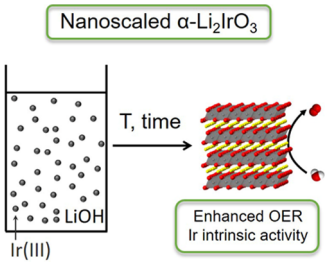

EXPERIMENTAL PROCEDURES

Synthesis. All reagents used in the synthesis were purchased from Aldrich, unless otherwise said, and used as received without further purification. Water used for washing is Milli-Q water.

LiIr-700: 100 mg of $IrCl_3{\cdot}xH_2O$ and 90 mg of $LiOH{\cdot}H_2O$ were grinded in an agate mortar and dried overnight at room temperature in a vacuum oven. The mixture was introduced in an alumina crucible and treated at 700 °C for 0.5 h in a preheated muffle oven in air atmosphere. Then, the reaction was quenched by removing the crucible from the hot oven.

LiIr-900: 100 mg of $IrCl_3{\cdot}xH_2O$ and 180 mg of $LiOH{\cdot}H_2O$ were grinded in an agate mortar and dried overnight at room temperature in a vacuum oven. The mixture was introduced in an alumina crucible and treated at 900 °C for 1 h in a preheated muffle oven in air atmosphere. Then, the reaction was quenched by removing the crucible from the hot oven.

Both materials were washed by centrifugation with deionized water several times until the conductance of the supernatant reached the value of water used for washing. The powder was dried under vacuum at room temperature overnight.

LiIr-ref: α-Li_2IrO_3 was obtained by a previously reported solid-state methodology.[1] Briefly, 1 mmol of Ir was grinded with 1.1 mmol of Li_2CO_3 and heated in two steps: 12 h hold at 1000 °C (heated at 5 °C/min) and 36 h hold at 900 °C (cooled by turning off the furnace). Between each step, the samples were ground and pressed back into pellets.

Material Characterization. Powder XRD was performed on a PANalytical Cubix'Pro diffractometer equipped with an X'Celerator detector and automatic divergence and reception slits using Cu−K_α radiation (0.154056 nm). Rietveld refinements were performed using the FullProf suite programs.[14]

The characterization by TEM was carried out on a Tecnai Spirit G2 apparatus operated at an accelerating voltage of 120 kV. High-angle annular dark-field scanning transmission electron microscopy (HAADF-STEM) was performed using a JEOL 2100F microscope with a probe aberration corrector.

Nitrogen adsorption−desorption isotherms were collected on a Micrometrics ASAP 2020 system at 77 K, after degassing the samples at 623 K under vacuum. The surface areas were calculated by the Brunauer−Emmett−Teller (BET) method, and pore size distribution was determined from the adsorption branch of the isotherm according to the Barrett-Joyner-Halenda (BJH) method.

XPS data were collected on a SPECS spectrometer equipped with a 150-MCD-9 detector and using a nonmonochromatic Al K_α (1486.6 eV) X-ray source. The binding energy (BE) values were referenced to C1s signal (284.6 eV). The spectral treatment has been performed using the CASA software.

To determine the lithium and iridium contents, the materials were dissolved under acid-oxidizing hydrothermal conditions following a previously described methodology.[15] An amount of 5 mg of the powder, 5 mL of HCl (37% w), and 200 μL of H_2O_2 (30% (w/w)) were introduced in a 35 mL teflon-lined autoclave at 200 °C for 15 h. The clear yellow solution obtained was diluted with Milli-Q water, and the contents of lithium and iridium were analyzed with a ThermoFisher iCAP PRO Series ICP-optical emission spectrometer.

FTIR analysis was performed using a PerkinElmer Spectrum 400 system.

Electrochemistry Measurements. A THF ink with a mass ratio of 5:1:1 of the catalyst to acetylene black to Nafion was sonicated for 30 min and drop-casted in a polished 5 mm diameter glassy carbon rotating disk electrode (RDE) with a loading of 0.256 mg_{cat} cm_{disk}^{-2} unless otherwise indicated. A three-electrode setup connected to a BioLogic MPG-30 potentiostat was employed to study the electrocatalytic properties. A Pt wire, a Ag/AgCl electrode calibrated with a reversible hydrogen electrode (HydroFlex, from Gaskatel, Germany), and the RDE with the deposited ink rotating at 1600 rpm were employed as the counter, reference, and working electrodes, respectively.

Li-ion batteries were assembled in an Ar-filled glovebox. LiIr-700, previously dried in a Buchi oven at 80 °C under vacuum overnight, was mixed with 20% weight of acetylene black carbon in a mortar. LP-100 (BASF) was used as the electrolyte, in which 1.0 M $LiPF_6$ is dissolved in EC/PC/DMC in a 1:1:3 weight ratio. Li-ion batteries were assembled using Swagelok-type cells with two glass fiber separators (Whatman, GF/D) and Li metal as the counter electrode. The assembled Li-ion cells were galvanostatically cycled using a VMP potentiostat (BioLogic S.A., Claix, France).

RESULTS AND DISCUSSION

Nanoscaled lithium iridates were synthesized through molten salt methodology by using $IrCl_3$ and LiOH as precursors. LiOH had dual action in the synthesis, solvent and reagent; thus, it melts at a relatively low temperature, allowing the dissolution of the $IrCl_3$ ionic precursor, avoids the coalescence of the particles, and acts as an oxygen and lithium provider. Following this procedure, two materials were prepared at two different temperatures, 700 °C (LiIr-700) and 900 °C (LiIr-900). Both materials are highly crystalline, as confirmed by the XRD analysis (Figure 1a). Both show peaks at the same position, confirming the same crystalline phase. The higher broadening of peaks of LiIr-700 samples further indicates the lower size of crystallites. Inspection of the peak position of this more crystalline material allowed to identify the crystalline phase, namely α-Li_2IrO_3. It further matched the pattern of the reference sample synthesized at a high-temperature solid-state reaction (LiIr-ref).[1] Rietveld refinement confirmed that the materials synthesized in molten salts are α-Li_2IrO_3 (Figure S1). In the case of Ir-700, a high population of defects, given the small crystal size, was observed, while in LiIr-900, minor secondary phases, similar to the main one, were detected (Table S1). The calculated crystallite size increases upon increasing the synthesis temperature from 2−3 to 12 nm for LiIr-700 and LiIr-900, respectively, while the lattice parameters a and c decrease (Tables S1 and S2).

https://doi.org/10.1021/acsanm.2c04949
ACS Appl. Nano Mater. 2023, 6, 2577−2584

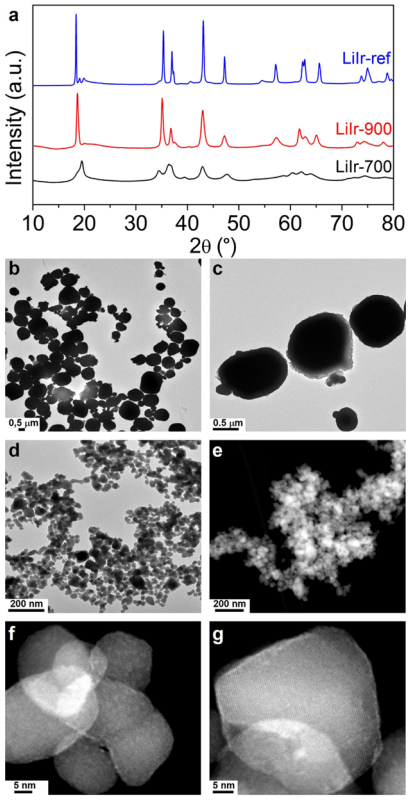

Figure 1. (a) XRD patterns of LiIr-ref, LiIr-900, and LiIr-700. (b, c) TEM images of LiIr-900. (d) TEM and (e–g) HAADF-STEM images of IrLi-700.

The difference in the crystallite size calculated by XRD is clearly visible in the TEM images. LiIr-900 shows dispersed particles of around 1 μm with spherical morphology (Figure 1b,c), while well-dispersed nanoparticles of around 40 nm are observed in LiIr-700 (Figure 1d–g). HAADF-STEM (Figure 1f,g) and HR-TEM (Figure S2) pictures show that the particles synthesized at 700 °C are composed by smaller crystalline domains of 5 nm. Similar behavior is observed in the sample obtained at 900 °C, when the XRD crystal and TEM particle sizes are compared. The observed polycrystalline nature of the particles explains the discrepancy between the crystallite and particle size. Additionally, the interplanar distance observed in the HR-TEM images of LiIr-700 is 0.48 nm, which corresponds to the {003} family planes of α-Li_2IrO_3 (Figure S2 and Table S2).

The difference in the particle size is reflected in the BET surface area, with LiIr-900 and LiIr-700 showing a specific surface area of 14 and 36 $m^2\ g^{-1}$, respectively (Figure S3). This is quite a remarkable result, taking into account the high mass of Ir and the density of the related compounds, which have a large impact on the BET surface area. Indeed, these surface area values are 2 orders of magnitude higher than those obtained for materials synthesized by the solid-state methodology.[5]

The lithium content in these kinds of materials is not usually reported, given the difficulties to quantify it; thus, it is too light to measure by EDX, and these compounds show high stability which makes their dissolution difficult in order to analyze by ICP. To determine the Li/Ir ratio by ICP, the materials were dissolved in acid-oxidizing media under hydrothermal conditions (see section Experimental Procedures).[15] The Li/Ir ratio for LiIr-700 was 1.1, lower than the expected composition of Li_2IrO_3, which can be explained by the small crystal size and the high amount of defects present that affects the stoichiometry. On the other side, the more crystalline LiIr-900 shows a composition closer than the expected one with a Li/Ir ratio of 2.3, while LiIr-ref shows a Li/Ir ratio of 3.6, higher than that expected, which indicates that unreacted lithium is left on the surface of this material during the synthesis.

The chemical nature of the species present on the surface was studied by XPS. Figure 2a,b shows the Ir 4f and O 1s XPS spectra of LiIr-700, LiIr-900, and LiIr-ref samples. The Ir 4f region consists of two main components ($4f_{7/2}$ and $4f_{5/2}$). Previous works on iridium oxides have reported the complexity to fit the Ir 4f core peaks because of the peculiar line shape.[16,17] As previously reported in similar materials, a good fit is obtained with two doublets coming from the final state effects and an additional component at the high binding energy[18] (Figure 2a). The Ir 4f envelope of LiIr-ref exhibits a peak shape associated to Ir+4 and hihger oxidation state (Ir $4f_{7/2}$ B.E.: 62.3 eV), in part due to the overlithiation of the material. For LiIr-900, the overall shape is rather the same (Ir $4f_{7/2}$ B.E.: 62.2 eV), and thus we can conclude to a mixed valency with Ir^{IV} and Ir in a higher oxidation state. However, for LiIr-700, the higher binding energy of the Ir $4f_{7/2}$ maximum (B.E.: 62.5 eV) leads to an increase in the whole Ir oxidation state with Ir^{IV} and a higher contribution of Ir in a higher oxidation state.

In the O 1s region, the components that appear at 530 and 531 eV correspond to the oxide and hydroxide species, respectively, while the components appearing at higher binding energies correspond to adsorbed water and adventitious carbon species[16,19–21] (Figure 2b). Similar relative hydroxide concentration is observed in the oxygen species region in both synthesized materials, while the relative amount of oxide species is higher in IrLi-700 (Table S3).

Comparing the FTIR spectra of both materials, LiIr-900 shows two intense peaks at 1422 and 866 cm^{-1}, which can be assigned to the asymmetric stretch (at about 1400 cm^{-1} (ν_3)) and out-of-plane bending absorption (at about 870 cm^{-1} (ν_2)) of carbonates,[22] while in LiIr-700, their intensity is almost negligible (Figure S4). Additionally, the C 1s XPS spectra of LiIr-900 show a higher area of the component located at 289.1 eV, corresponding to the carbonates[23] (IrLi-700 (2.9% at) and LiIr-900 (23.2% at)), compared to the adventitious carbon component (284.6 eV, similar atomic percentage in both samples), while the amount of iridium is lower (IrLi-700 (35.1% at) and LiIr-900 (13.3% at)) (Figure S5 and Table S4). All these suggest a higher relative concentration of surface carbonates in LiIr-900. These carbonates may partially block the accessibility of the oxide species to the XPS technique (depth ~5–10 nm), explaining the lower relative concentration of this species in IrLi-900 compared to LiIr-700. Additionally, compared to both previous samples, LiIr-ref shows a lower percentage of hydroxide species and a higher relative concentration of oxide ones. This may arise from the higher temperature employed in the synthesis, which yields a bigger particle size and hence lower hydroxide concentration on the surface.

The electrocatalytic behavior of lithium iridates has been related to de-insertion of lithium.[5] As in previous works, α-Li_2IrO_3 obtained by the solid-state methodology shows an irreversible oxidation peak in the first scan upon positive electrode polarization in basic oxygen evolution reaction

https://doi.org/10.1021/acsanm.2c04949
ACS Appl. Nano Mater. 2023, 6, 2577–2584

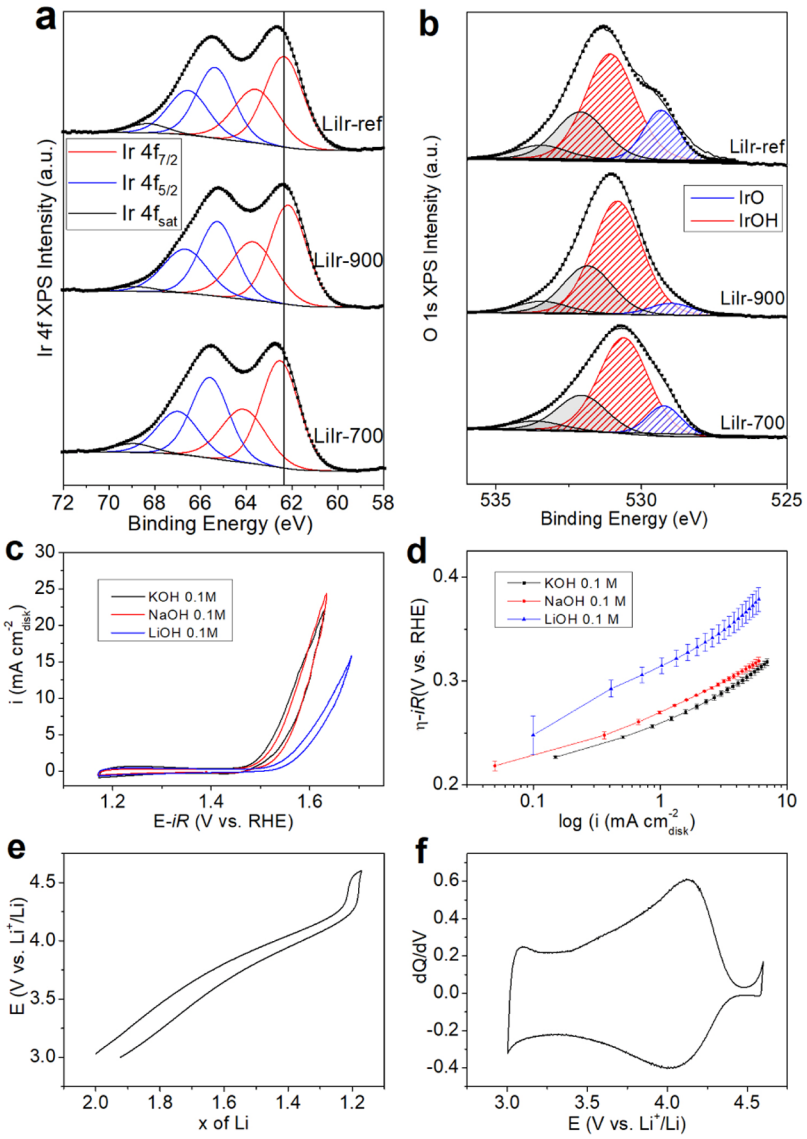

Figure 2. (a) Ir 4f and (b) O 1s XPS spectra of LiIr-700, LiIr-900, and IrLi-ref. (c) CV curves in KOH, NaOH, and LiOH, 0.1 M and (d) corresponding Tafel plots of LiIr-700. (e) Cycling curve of LiIr-700 as a Li-ion battery electrode in an organic solvent and (f) CV curve obtained from a galvanostatic charge by applying the derivate.

(OER) conditions (Figure S6a−c). This wave corresponds to the formation of α-Li_1IrO_3 that in the presence of potassium coming from the electrolyte evolves to $Li_xK_{0.3}IrO_3{\cdot}0.7H_2O$ with a birnessite structure. This phase evolution occurs only in the KOH electrolyte (neither in NaOH nor in LiOH is observed), and the phase obtained shows high activity and stability in OER.[5]

The OER properties of the materials synthesized were studied in basic electrolytes. LiIr-700 shows the highest activity in OER in KOH, followed by NaOH and LiOH (Figure 2c,d). As before, LiIr-900 and LiIr-ref show the same electrolyte activity trend (Figure S7). Comparing the electrocatalytic activity of the several materials synthesized, the higher the synthesis temperature the lower is the current achieved (Figure S8), which may be related to the bigger crystal size leading to lower number of active sites available. Curiously, none of the new materials obtained in this work show an irreversible oxidation peak around 1.23 V versus RHE in the first scan, characteristic of α-Li_1IrO_3 formation.

Higher amounts of the ink containing the electrocatalyst were deposited on a gas diffusion layer (GDL) and cycled in different electrolytes to study the structural evolution. No appreciable difference was observed between the noncycled and cycled materials (Figure S9a,b), and no peak appeared around 2θ = 13°, which would indicate the birnessite phase formation, as that occurs when bulk α-Li_2IrO_3 is cycled in KOH. The same experiment was performed depositing on a glassy carbon (GC) the same ink loading as that used in RDE, and the XRD of the GC was subtracted in order to appreciate more clearly the XRD peaks of LiIr-700. Interestingly, these XRD patterns (Figure S10a) showed the same profile as that of the pristine material. Additionally, 50 mg of LiIr-700 was ex situ-oxidized with an excess of ammonium persulfate (0.88 mmol) in the corresponding electrolytes at 1 M concentration. After ex situ oxidation, the solution shows a brownish orange color, indicating Ir leaching, which is removed in the first centrifugation, leading to transparent washing waters in the following ones. These ex situ-oxidized materials show the same XRD patterns as that of the fresh materials (Figure S10b),

https://doi.org/10.1021/acsanm.2c04949
ACS Appl. Nano Mater. 2023, 6, 2577−2584

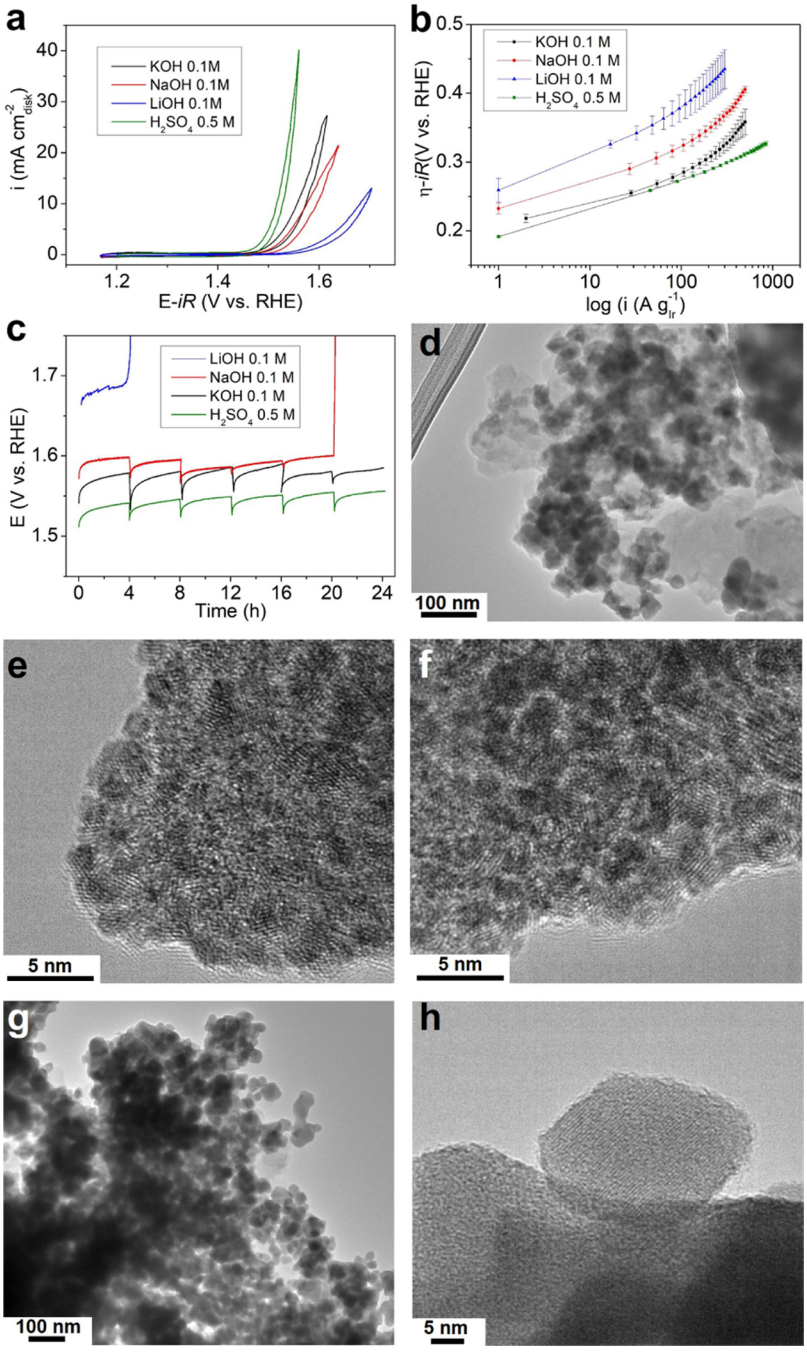

Figure 3. (a) CV curves in KOH, NaOH, LiOH 0.1 M, and H_2SO_4 0.5 M of IrLi-700 (0.076 mg_{cat} cm_{disk}^{-2} loading) and (b) corresponding iridium mass-normalized Tafel slopes. (c) Chronopotentiometry curves of IrLi-700 in the KOH, NaOH, LiOH 0.1 M, and H_2SO_4 0.5 M electrolytes at 5 mA cm_{disk}^{-2}. TEM images of IrLi-700 after chronopotentiometry in (d–f) KOH 0.1 M and (g, h) H_2SO_4 0.5 M.

while almost no detectable potassium and 0.22 sodium per iridium were observed by EDX in the materials oxidized in KOH and NaOH, respectively. Additionally, the GC-deposited inks were recovered, dissolved, and the lithium content analyzed by ICP. Interestingly, the materials cycled in KOH and NaOH showed an iridium/lithium ratio of 1.0 and 0.6, respectively, indicating a small lithium loss compared to the pristine material and the possible formation of α-Li_1IrO_3. Additionally, the material cycled in acidic conditions showed almost no detectable lithium, suggesting that lithium in the structure is replaced by the protons of the electrolyte.

All in all, these materials show no phase evolution and incorporation of potassium which would be indicated by the detection of the birnessite phase. Further information about the insertion–deinsertion capacity of Li ions can be studied by cycling them in organic solvents; thus, partially or completely delithiated phases can be isolated in this water and oxygen-free conditions, allowing to track their reactivity in other environments, which in some cases produce new phases with excellent electrocatalytic activity.[4,5]

LiIr-700 cycled in organic solvents shows no plateau at 3.5 V versus Li^+/Li, corresponding to the formation of α-Li_1IrO_3[5] (Figure 2e). The absence of the plateau is characteristic of

https://doi.org/10.1021/acsanm.2c04949
ACS Appl. Nano Mater. 2023, 6, 2577–2584

nanomaterials in which large fractions of Li^+ storage sites are on the surface or near-surface region.[24,25] CV curves obtained from the galvanostatic charge by applying the derivate show oxidation and reduction peaks (Figure 2f), confirming that this material still behaves as a battery material, even though the extrinsic pseudocapacitance is derived from the nanometric size and the large surface area where Li^+ can be stored.[25]

The lithium iridates obtained in this work, though showing the highest activity in the KOH electrolyte, do not show the irreversible oxidation peak around 1.23 V versus RHE observed in the bulk phase, indicative of α-Li_1IrO_3 formation. The structural and compositional analyses of the postcycled and ex situ-oxidized materials show a small lithium loss and a material composition near α-Li_1IrO_3, preserving the pristine structure with no incorporation of potassium. CV cycling in organic solvents shows no plateau characteristic of phase transformation, though it shows a battery material behavior. The absence of the oxidation wave during OER and the plateau in the CV cycling in organic solvents is indicative that the process is not limited by diffusion. The small size and the high number of defects may provoke that the delithiation curve does not show any well-defined redox peak or plateau, and the hydrated potassium might not react as much as for well-crystalline materials.

The order of activity observed in these basic electrolytes has been previously reported and has been ascribed to the differences in the water ordering capacity of the cation in the electrolyte, governed by its charge/radius ratio. In this sense, water molecules in the hydration shell are more ordered in the smaller cations than in the bigger ones, resulting in lower stabilized oxygen intermediates which render improved kinetics when K^+ is employed as a cation in the basic electrolyte compared to the smaller ones as Li^+.[26]

The OER properties of these materials were also studied in acid electrolytes (H_2SO_4 0.5 M). LiIr-ref shows a peak centered at 1.23 V versus RHE during the first scan (Figure S6d), suggesting α-Li_1IrO_3 formation, as in basic conditions. Neither LiIr-700 nor LiIr-900 shows this oxidation peak, behaving as before in basic electrolytes. CV results show that both materials synthesized in molten salts show similar overpotential values, though showing much different surface area values, while LiIr-ref shows the lowest activity (Figure S11).

Current normalized by surface area values is traditionally accepted as a good approximation for comparing the intrinsic electrocatalytic activity of materials with different compositions, even if the real number of active sites may not be fully proportional to the surface area. Additionally, materials obtained by solid-state methodology show extremely low surface area values, which makes the accurate BET surface area determination difficult. Moreover, the structure-evolving nature of some electrocatalysts under reaction conditions precludes the use of the pristine surface area value, making its measurement in the evolved material necessary,[27] which in some cases is difficult to isolate. All these compromise the catalyst activity comparison by this methodology.

Current normalized by the electrode iridium content is, unlike that normalized by the surface area, an interesting way of comparing the intrinsic activity of electrocatalysts, given the scarcity and the high price of this element, and can give a better idea of the real use of iridium in the electrode. The ink amount in the electrode was optimized, thus decreasing the amount of IrLi-700 to 0.076 mg_{cat} cm_{disk}^{-2}, almost equal to the current values obtained with the former catalyst electrode loading (0.256 mg_{cat} cm_{disk}^{-2}) in the four electrolytes (Figure 3a), indicating that some particles were not electrocatalytically accessible because of the film thickness. Further decreasing the amount of ink decreased the current values achieved at the same potential.

The order of activity in basic media followed the previous one, with KOH being the more active, followed by NaOH and LiOH (Figure 3a), with an intrinsic mass activity of 181, 40, and 6 A g_{Ir}^{-1} at an overpotential of 0.3 V versuss RHE, respectively (Figure 3b). Better values are obtained in acid media, giving a mass activity of 336 A g_{Ir}^{-1}, comparable with one of the most active iridium-based catalysts such as IrO_x[28] or exfoliated hydrated $H_{3.6}IrO_4{\cdot}3.7H_2O$[27] and only surpassed by nano core−shell $IrNiO_x$[29] catalysts and hafnium-modified iridium oxide ($IrHf_xO_y$)[30] (Figure 3b). This high-intrinsic mass activity may arise from the small crystal size that this material shows with a higher number of exposed surface atoms and hence higher number of catalytic active sites.

The stability of LiIr-700 was assessed in different electrolytes. For this purpose, chronopotentiometry at 5 mA cm_{disk}^{-2}, the same value reported in similar experiments for bulk α-Li_1IrO_3 in basic electrolytes,[5] was performed with a catalyst loading of 0.076 mg_{cat} cm_{disk}^{-2} in order to appreciate any catalyst deactivation (Figure 3c). The potential required to reach the proposed current in the H_2SO_4 0.5 M electrolyte is centered at 1.53 V versus RHE with a slight deactivation (below 2%) after 24 h (Figures 3c and S12g,h). Similar behavior is observed in KOH, with an average potential of 1.56 V versus RHE and a slight deactivation (Figures 3c and S12a,b). In NaOH, the required potential is 1.59 V versus RHE, and the material is relatively stable until 20 h, where a drastic increase in the potential is observed (Figures 3c and S12c,d). A higher potential is needed in LiOH (1.68 V vs RHE), and the materials show low stability; thus, after 4 h, the potential required drastically increased (Figures 3c and S12e,f). After chronoamperometry, it was possible to recover only the catalyst tested in H_2SO_4 and KOH; thus, no catalyst was present in the RDE after these experiments in NaOH and LiOH electrolytes. The TEM images of LiIr-700 after the chronopotentiometry test in H_2SO_4 and KOH show that the particle size is preserved (Figure 3d−h). After the stability test in KOH, the roughness of the particle surface increases, making easy the observation of the small nanocrystals that form them (Figure 3d−f). Contrarily, in H_2SO_4, the particles keep the smooth surface as that of the pristine material, though still showing some crystallinity; this is not so evident as in the materials tested in KOH (Figure 3g,h).

CONCLUSIONS

Nanostructured lithium iridates have been synthesized in molten salts with tunable particle and crystal sizes for the first time. The iridium ionic precursor and the solvent that acts as a lithium and oxygen provider preclude the particle growth and allow the colloidal synthesis at the required high temperature. The structural analysis confirmed that these materials were composed by α-Li_2IrO_3 structure with a surface area 2 orders of magnitude higher than that of the materials obtained by traditional solid-state methodology. Another consequence of the small crystal size of these materials is the presence of defects, which has consequences in the stoichiometry; thus, lithium content lower than that of the theoretical one was

https://doi.org/10.1021/acsanm.2c04949
ACS Appl. Nano Mater. 2023, 6, 2577−2584

observed, besides showing Ir^{IV} and a higher contribution of Ir in a higher oxidation state in the structure.

Improved OER activities were obtained compared to the bulk counterpart, given the improved surface area. Intriguingly, the electrocatalytic behavior of this nanoscaled α-Li_2IrO_3 significantly differs from that of the bulk counterpart; thus, neither the oxidation peak during the first OER scan at 1.23 V versus RHE nor the plateau at 3.5 V versus Li^+/Li when it is cycled in organic solvents is observed, and no potassium-based birnessite phase, when cycled in the KOH electrolyte, is detected. Such a different behavior compared to that of the bulk counterpart may arise from the small size of the materials synthesized, and the high number of defects that provoke the delithiation curve does not show any well-defined redox peak or plateau, and the hydrated potassium might not react as much as that for well-crystalline materials. Hence, the reactions that occur are not limited by cation diffusion in the material, playing a key role in the redox reactions on the surface.

Additionally, the nanoscaled α-Li_2IrO_3 shows good chemical and structural stability; thus, negligible deactivation was observed in KOH and H_2SO_4 electrolytes with a low electrode catalyst loading during 24 h of chronopotentiometry. Besides this stability, these materials show enhanced iridium intrinsic activity with 336 and 181 A g_{Ir}^{-1} in H_2SO_4 and KOH electrolytes, respectively.

This works shows how the design of high-temperature colloidal synthesis yields nanoscaled materials with enhanced and different electrocatalytic properties compared to bulk counterparts and paves the way to the design of new electrocatalysts with enhanced mass activity.

■ ASSOCIATED CONTENT

Supporting Information

The Supporting Information is available free of charge at https://pubs.acs.org/doi/10.1021/acsanm.2c04949.

Characterization of the materials and electrocatalytic results (PDF)

■ AUTHOR INFORMATION

Corresponding Authors

Francisco Gonell − *CNRS, Collège de France, Laboratoire de Chimie de la Matière Condensée de Paris (LCMCP), Sorbonne Université, Paris F-75005, France;* Present Address: Instituto de Tecnología Química (UPV-CSIC), Universitat Politècnica de València-Consejo Superior de Investigaciones Científicas, Avda. de los Naranjos s/n, 46022 Valencia, Spain; orcid.org/0000-0002-8658-2878; Email: fgonell@itq.upv.es

Clément Sanchez − *CNRS, Collège de France, Laboratoire de Chimie de la Matière Condensée de Paris (LCMCP), Sorbonne Université, Paris F-75005, France; USIAS, Université de Strasbourg Institut d'Études Avancés, Strasbourg 67000, France;* orcid.org/0000-0002-6426-4844; Email: clement.sanchez@upmc.fr

Authors

Gwenaëlle Rousse − *Chimie du Solide et de l'Energie, Collège de France UMR 8260, Paris 7523, France; Réseau sur le Stockage Electrochimique de l'Energie (RS2E), CNRS FR 3459, Cedex Amiens 80039, France; Sorbonne Université, Paris F-75005, France;* orcid.org/0000-0001-8877-0015

Mateusz Odziomek − *CNRS, Collège de France, Laboratoire de Chimie de la Matière Condensée de Paris (LCMCP), Sorbonne Université, Paris F-75005, France;* Present Address: Max Planck Institute of Colloids and Interfaces, Am Muehlenberg 1, 14476 Potsdam, Germany

Walid Baaziz − *IPCMS, UMR 7504 CNRS-Université de Strasbourg, Strasbourg Cedex 2 67034, France*

Ovidiu Ersen − *IPCMS, UMR 7504 CNRS-Université de Strasbourg, Strasbourg Cedex 2 67034, France;* orcid.org/0000-0002-1553-0915

Alexis Grimaud − *Chimie du Solide et de l'Energie, Collège de France UMR 8260, Paris 7523, France; Réseau sur le Stockage Electrochimique de l'Energie (RS2E), CNRS FR 3459, Cedex Amiens 80039, France;* orcid.org/0000-0002-9966-205X

Complete contact information is available at: https://pubs.acs.org/10.1021/acsanm.2c04949

Notes

The authors declare no competing financial interest.

■ ACKNOWLEDGMENTS

Fondation Collège de France has supported this work.

■ REFERENCES

(1) McCalla, E.; Abakumov, A. M.; Saubanere, M.; Foix, D.; Berg, E. J.; Rousse, G.; Doublet, M.-L.; Gonbeau, D.; Novak, P.; Van Tendeloo, G.; Dominko, R.; Tarascon, J.-M. Visualization of O-O Peroxo-like Dimers in High-Capacity Layered Oxides for Li-Ion Batteries. *Science* **2015**, *350*, 1516−1521.

(2) Pearce, P. E.; Perez, A. J.; Rousse, G.; Saubanère, M.; Batuk, D.; Foix, D.; McCalla, E.; Abakumov, A. M.; Van Tendeloo, G.; Doublet, M.-L.; Tarascon, J.-M. Evidence for Anionic Redox Activity in a Tridimensional-Ordered Li-Rich Positive Electrode β-Li2IrO3. *Nat. Mater.* **2017**, *16*, 580−586.

(3) Perez, A. J.; Jacquet, Q.; Batuk, D.; Iadecola, A.; Saubanère, M.; Rousse, G.; Larcher, D.; Vezin, H.; Doublet, M.-L.; Tarascon, J.-M. Approaching the Limits of Cationic and Anionic Electrochemical Activity with the Li-Rich Layered Rocksalt Li3IrO4. *Nat. Energy* **2017**, *2*, 954−962.

(4) Pearce, P. E.; Yang, C.; Iadecola, A.; Rodriguez-Carvajal, J.; Rousse, G.; Dedryvère, R.; Abakumov, A. M.; Giaume, D.; Deschamps, M.; Tarascon, J.; Grimaud, A. Revealing the Reactivity of the Iridium Trioxide Intermediate for the Oxygen Evolution Reaction in Acidic Media. *Chem. Mater.* **2019**, *31*, 5845−5855.

(5) Yang, C.; Rousse, G.; Louise Svane, K.; Pearce, P. E.; Abakumov, A. M.; Deschamps, M.; Cibin, G.; Chadwick, A. V.; Dalla Corte, D. A.; Anton Hansen, H.; Vegge, T.; Tarascon, J.; Grimaud, A. Cation Insertion to Break the Activity/Stability Relationship for Highly Active Oxygen Evolution Reaction Catalyst. *Nat. Commun.* **2020**, *11*, 1378.

(6) Bojdys, M. J.; Wohlgemuth, S. A.; Thomas, A.; Antonietti, M. Ionothermal Route to Layered Two-Dimensional Polymer-Frameworks Based on Heptazine Linkers. *Macromolecules* **2010**, *43*, 6639−6645.

(7) Bojdys, M. J.; Müller, J.-O.; Antonietti, M.; Thomas, A. Ionothermal Synthesis of Crystalline, Condensed, Graphitic Carbon Nitride. *Chem. − Eur. J.* **2008**, *14*, 8177−8182.

(8) Liu, X.; Fechler, N.; Antonietti, M. Salt Melt Synthesis of Ceramics, Semiconductors and Carbon Nanostructures. *Chem. Soc. Rev.* **2013**, *42*, 8237.

(9) Gonell, F.; Sanchez-Sanchez, C. M.; Vivier, V.; Méthivier, C.; Laberty-Robert, C.; Portehault, D. Structure-Activity Relationship in Manganese Perovskite Oxide Nanocrystals from Molten Salts for Efficient Oxygen Reduction Reaction Electrocatalysis. *Chem. Mater.* **2020**, *32*, 4241−4247.

(10) Gonell, F.; Sanchez-Sanchez, C. M.; Vivier, V.; Laberty-Robert, C.; Portehault, D. Experimental Descriptors for the Synthesis of Multicationic Nickel Perovskite Nanoparticles for Oxygen Reduction. *ACS Appl. Nano Mater* **2020**, *3* (8), 7482−7489.
(11) Kumar, R.; Bahri, M.; Song, Y.; Gonell, F.; Thomas, C.; Ersen, O.; Sanchez, C.; Laberty-Robert, C.; Portehault, D. Phase Selective Synthesis of Nickel Silicide Nanocrystals in Molten Salts for Electrocatalysis of the Oxygen Evolution Reaction. *Nanoscale* **2020**, *12*, 15209−15213.
(12) Portehault, D.; Devi, S.; Beaunier, P.; Gervais, C.; Giordano, C.; Sanchez, C.; Antonietti, M. A General Solution Route toward Metal Boride Nanocrystals. *Angew. Chem., Int. Ed.* **2011**, *50*, 3262−3265.
(13) Thi N'Goc, H.; Mouafo, L. D. N.; Etrillard, C.; Torres-Pardo, A.; Dayen, J.-F.; Rano, S.; Rousse, G.; Laberty-Robert, C.; Calbet, J. G.; Drillon, M.; Sanchez, C.; Doudin, B.; Portehault, D. Surface-Driven Magnetotransport in Perovskite Nanocrystals. *Adv. Mater.* **2017**, *29*, No. 1604745.
(14) Rodriguez-Carvajal, J. H. FullProf Suite. All the programs can be obtained from: https://www.ill.eu/sites/fullprof/php/programs.html.
(15) Hodgson, A. P. J.; Jarvis, K. E.; Grimes, R. W.; Marsden, O. J. Development of an Iridium Dissolution Method for the Evaluation of Potential Radiological Device Materials. *J. Radioanal. Nucl. Chem.* **2016**, *307*, 2181−2186.
(16) Abbott, D. F.; Lebedev, D.; Waltar, K.; Povia, M.; Nachtegaal, M.; Fabbri, E.; Copéret, C.; Schmidt, T. J. Iridium Oxide for the Oxygen Evolution Reaction: Correlation between Particle Size, Morphology, and the Surface Hydroxo Layer from Operando XAS. *Chem. Mater.* **2016**, *28*, 6591−6604.
(17) Pfeifer, V.; Jones, T. E.; Velasco Vélez, J. J.; Massué, C.; Arrigo, R.; Teschner, D.; Girgsdies, F.; Scherzer, M.; Greiner, M. T.; Allan, J.; Hashagen, M.; Weinberg, G.; Piccinin, S.; Hävecker, M.; Knop-Gericke, A.; Schlögl, R. The Electronic Structure of Iridium and Its Oxides. *Surf. Interface Anal.* **2016**, *48*, 261−273.
(18) Foix, D.; Sathiya, M.; McCalla, E.; Tarascon, J.-M.; Gonbeau, D. X-Ray Photoemission Spectroscopy Study of Cationic and Anionic Redox Processes in High-Capacity Li-Ion Battery Layered-Oxide Electrodes. *J. Phys. Chem. C* **2016**, *120*, 862−874.
(19) Kötz, R.; Neff, H.; Stucki, S. Anodic Iridium Oxide Films: XPS-Studies of Oxidation State Changes and O2 Evolution. *J. Electrochem. Soc.* **1984**, *131*, 72.
(20) Saveleva, V. A.; Wang, L.; Teschner, D.; Jones, T.; Gago, A. S.; Friedrich, K. A.; Zafeiratos, S.; Schlögl, R.; Savinova, E. R. Operando Evidence for a Universal Oxygen Evolution Mechanism on Thermal and Electrochemical Iridium Oxides. *J. Phys. Chem. Lett.* **2018**, *9*, 3154−3160.
(21) Smith, R. D. L.; Sporinova, B.; Fagan, R. D.; Trudel, S.; Berlinguette, C. P. Facile Photochemical Preparation of Amorphous Iridium Oxide Films for Water Oxidation Catalysis. *Chem. Mater.* **2014**, *26*, 1654−1659.
(22) Cai, G.-B.; Chen, S.-F.; Liu, L.; Jiang, J.; Yao, H.-B.; Xu, A.-W.; Yu, S.-H. 1,3-Diamino-2-Hydroxypropane-N,N,N′,N′-Tetraacetic Acid Stabilized Amorphous Calcium Carbonate: Nucleation, Transformation and Crystal Growth. *CrystEngComm* **2010**, *12*, 234−241.
(23) Stoch, J.; Gablankowska-Kukucz, J. The Effect of Carbonate Contaminations on the XPS O 1s Band Structure in Metal Oxides. *Surf. Interface Anal.* **1991**, *17*, 165−167.
(24) Okubo, M.; Hosono, E.; Kim, J.; Enomoto, M.; Kojima, N.; Kudo, T.; Zhou, H.; Honma, I. Nanosize Effect on High-Rate Li-Ion Intercalation in LiCoO2 Electrode. *J. Am. Chem. Soc.* **2007**, *129*, 7444−7452.
(25) Simon, P.; Gogotsi, Y.; Dunn, B. Where Do Batteries End and Supercapacitors Begin? *Science* **2014**, *343*, 1210−1211.
(26) Rao, R. R.; Huang, B.; Katayama, Y.; Hwang, J.; Kawaguchi, T.; Lunger, J. R.; Peng, J.; Zhang, Y.; Morinaga, A.; Zhou, H.; You, H.; Shao-Horn, Y. PH- and Cation-Dependent Water Oxidation on Rutile RuO 2 (110). *J. Phys. Chem. C* **2021**, *125*, 8195−8207.
(27) Zhang, R.; Pearce, P. E.; Pimenta, V.; Cabana, J.; Li, H.; Alves Dalla Corte, D.; Abakumov, A. M.; Rousse, G.; Giaume, D.; Deschamps, M.; Grimaud, A. First Example of Protonation of Ruddlesden−Popper Sr 2 IrO 4: A Route to Enhanced Water Oxidation Catalysts. *Chem. Mater.* **2020**, *32*, 3499−3509.
(28) Lettenmeier, P.; Majchel, J.; Wang, L.; Saveleva, V. A.; Zafeiratos, S.; Savinova, E. R.; Gallet, J.-J.; Bournel, F.; Gago, A. S.; Friedrich, K. A. Highly Active Nano-Sized Iridium Catalysts: Synthesis and Operando Spectroscopy in a Proton Exchange Membrane Electrolyzer. *Chem. Sci.* **2018**, *9*, 3570−3579.
(29) Nong, H. N.; Reier, T.; Oh, H.-S.; Gliech, M.; Paciok, P.; Vu, T. H. T.; Teschner, D.; Heggen, M.; Petkov, V.; Schlögl, R.; Jones, T.; Strasser, P. A Unique Oxygen Ligand Environment Facilitates Water Oxidation in Hole-Doped IrNiOx Core−Shell Electrocatalysts. *Nat. Catal.* **2018**, *1*, 841−851.
(30) Zhao, F.; Wen, B.; Niu, W.; Chen, Z.; Yan, C.; Selloni, A.; Tully, C. G.; Yang, X.; Koel, B. E. Increasing Iridium Oxide Activity for the Oxygen Evolution Reaction with Hafnium Modification. *J. Am. Chem. Soc.* **2021**, *143* (38), 15616−15623.

https://doi.org/10.1021/acsanm.2c04949
ACS Appl. Nano Mater. 2023, 6, 2577−2584